FIGURE 9 Maps of horizontal and vertical displacement of the quasi-incompressible Cook membrane test, for the hybrid equilibrium element with quadratic stress field (HEE2), cubic stress field (HEE3), quartic stress field (HEE4) and for the nine-node displacement-based element (Q9), with meshes of 8×12 elements

4.2.1 | Slow axial pulse load

The numerical simulation of elastic-dynamic analysis of the cantilever beam subjected to the uniform axial load $\boldsymbol{p}_n$ is applied by the time continuous loading law $f_1(t)$ represented in Figure 11, with the greater value of pulse load application time: $\Delta T_1 = 8$ s, with constant time increment $\Delta t = \Delta T_1/160 = 5 \cdot 10^{-2}$ s and with $t_{max} = 50$ s.

The results of the dynamic analysis obtained with the coarse meshes of the dynamic HEE formulation and with the standard DB one, are compared in Figure 12A in terms of horizontal and vertical displacements and in terms of normal stress σ_x, at point B represented in Figure 12B. The four different solutions (HHE2, HEE3, HEE4, and Q9) are practically coincident in terms of horizontal displacement u_x at point B, whereas some small differences can be observed in terms of the vertical component u_y, especially in the HEE2 formulation. This error is probably due to the asymmetry of the HEE meshes. Conversely, the HEE formulation computes the exact value of the normal stress σ_x at point B, which is imposed as a boundary condition, and the DB formulation produces non null stress values after the pulse load, when the right end is unloaded and null normal stress is expected. The differences between the HEE and DB formulations are very small and vanish completely with the fine meshes, so that it can be stated that the two formulations converge to the exact elastic dynamic solution.

4.2.2 | Fast axial pulse load

The differences between the two formulations are more pronounced for the faster pulse load, which is defined by the continuous loading law $\boldsymbol{p}_n f_1(t)$ with $\Delta T = 0.08$ s, with constant time increment $\Delta t = \Delta T_2/160 = 5 \cdot 10^{-4}$ s and with $t_{max} = 0.50$ s. The relevant numerical results, obtained with coarse and fine meshes, with the quadratic, cubic, and quartic HEE
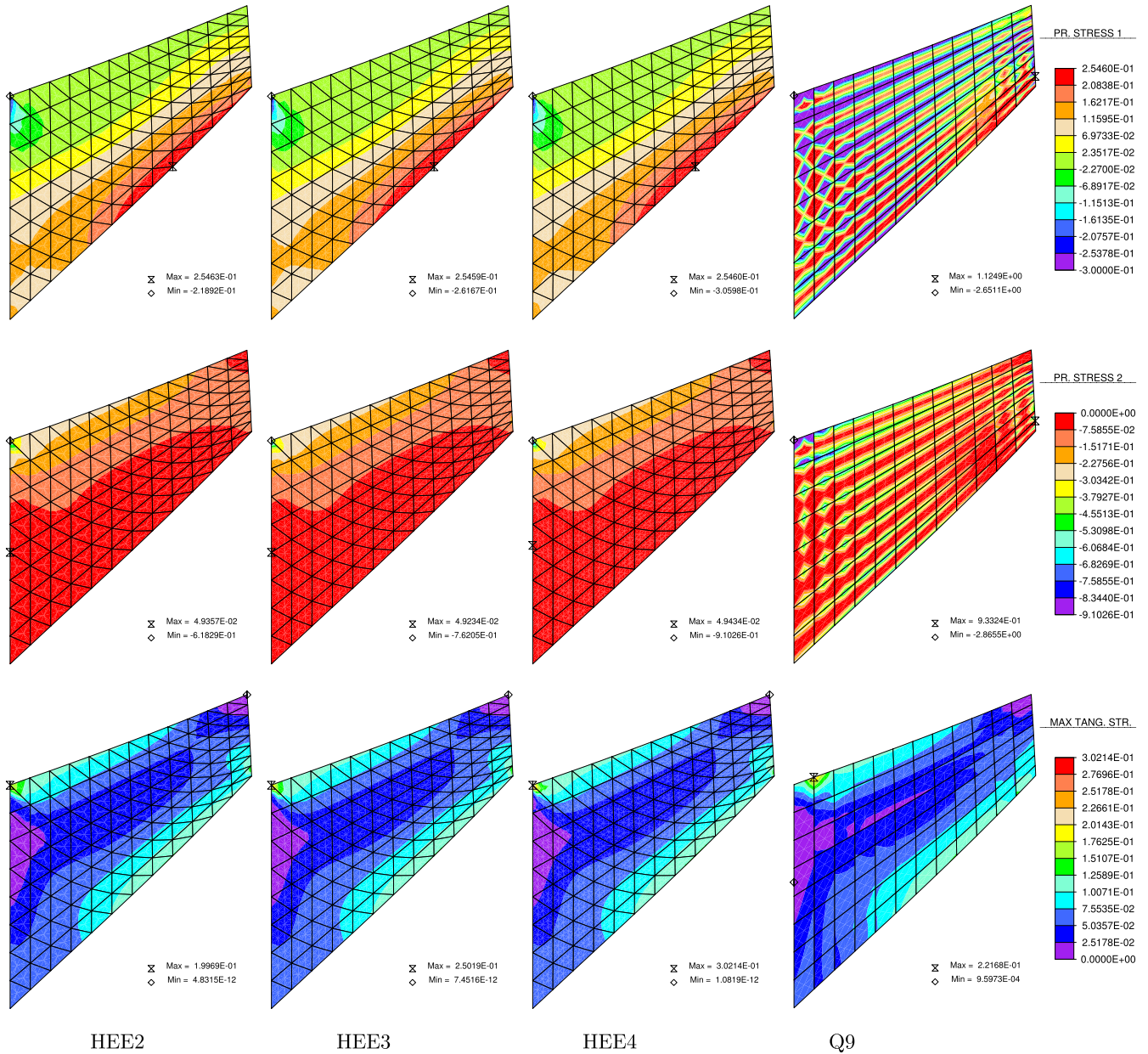
FIGURE 10 Maps of principal stresses and maximum tangential stress of quasi-incompressible Cook membrane test, for the hybrid equilibrium element with quadratic stress field (HEE2), cubic stress field (HEE3), quartic stress field (HEE4) and for the nine-node displacement-based element (Q9), with meshes of 8×12 elements

formulations and with the DB one are compared in Figure 13 in terms of horizontal and vertical displacement components at point A in the time domain.

The numerical solutions are also compared in Figure 14A–D in terms of evolution of stress components at point B in the time domain. The stress components σ_x and τ_{xy} are imposed as a boundary condition in the HEE formulations and coincide to the exact solutions for both coarse meshes and fine meshes. The DB solution provides some small errors in terms of stress which become negligible with the fine mesh. Finally, the evolution in the time domain of normal stress σ_y, which is not imposed as a boundary condition in HEE formulation, is plotted in Figure 14B for the coarse mesh, with some differences between the different solutions, and in Figure 14D for the fine mesh, showing perfectly coincident results and convergence of the two formulations to the exact solution. In this sense, the proposed dynamic equilibrium-based formulation can also be considered as a dual approach for the error estimation and for the convergence analysis of the classic DB approach.
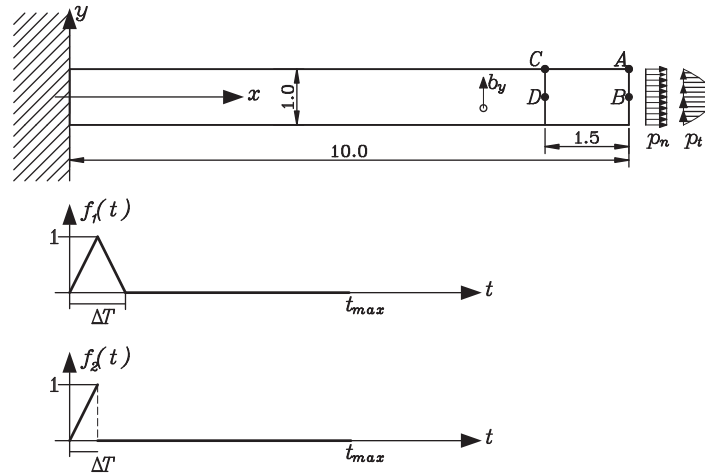
FIGURE 11 The cantilever beam dynamic test with the three load setting: the axial uniform pressure $\boldsymbol{p}_n$, the quadratic tangential pressure $\boldsymbol{p}_t$, and the vertical body force b_y. The loads are applied as dynamic pulse by the continuous loading law $f_1(t)$ and the discontinuous loading law $f_2(t)$

TABLE 2 Details of the discretizations employed in the dynamic analysis of the cantilever beam, with the hybrid equilibrium element and with the DB nine-nodes element

| HEE2		HEE3		HEE4		Q9	
Mesh	No. nodes	Mesh	No. nodes	Mesh	No. nodes	Mesh	No. nodes
2×20	426	2×20	568	2×20	710	2×20	205
10×100	9330	10×100	12,440	10×100	15,550	16×160	10,593
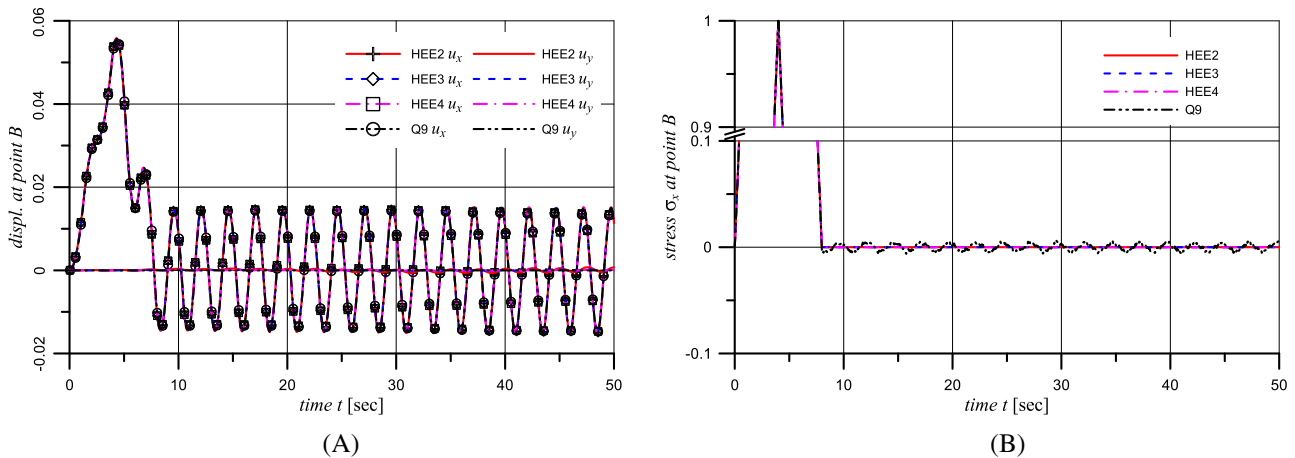
FIGURE 12 Dynamic response of a cantilever beam subjected to a slow pulse axial load $\boldsymbol{p}_n f_1(t)$ ($\Delta T = 8$ s), for the quadratic, cubic, and quartic HEEs and for the nine-node DB element, with coarse 2×10 meshes, in terms of (A) horizontal and vertical displacement at point B; (B) normal stress σ_x at point B

The maps of horizontal displacement u_x and the maps of normal stress σ_x, at time $t = 16.0$ s, computed with the HEE formulation and the DB approach with coarse and fine meshes are plotted respectively in Figures 15 and 16. There it can be observed that displacement and stress computed with the coarse meshes do not coincide with each other and the equilibrium-based solutions do not show a symmetric response, due to the asymmetry of the HEE meshes. Moreover, some displacement discontinuity between coincident nodes is noticeable in the solution with quadratic stress fields (HEE2) but vanishes altogether with higher stress fields (HEE3 and HEE4). The numerical results for the fine meshes respect the symmetry condition of the axial load and are all perfectly coincident in terms of both displacement and stress,

coarse mesh   fine mesh
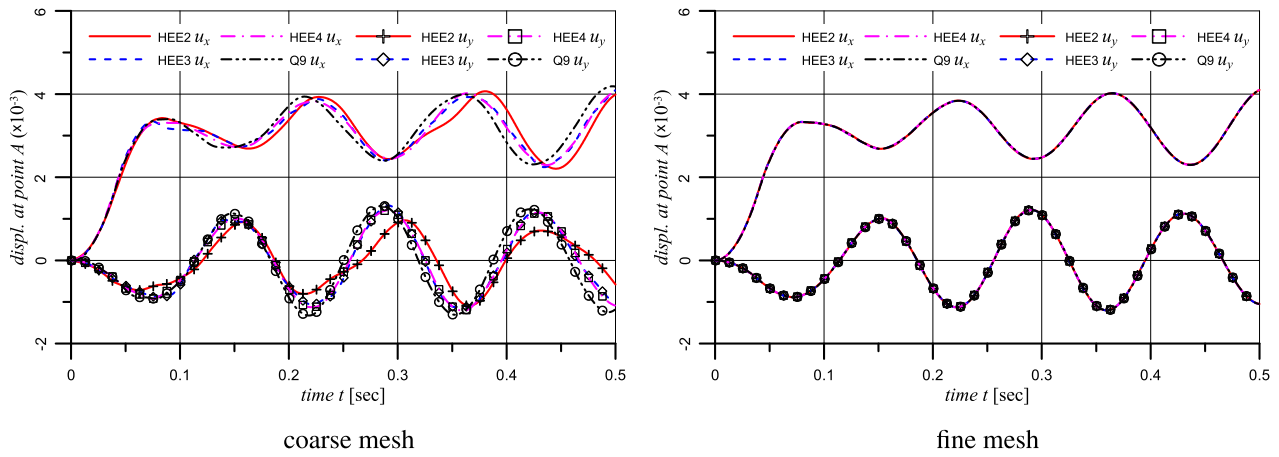
FIGURE 13   Dynamic response of a cantilever beam subjected to the fast axial pulse load $\boldsymbol{p}_n f_1(t)$ ($\Delta T = 0.08$ s), in terms of vertical and horizontal displacement at point A, for the quadratic, cubic, and quartic HEE and for the nine-node DB element
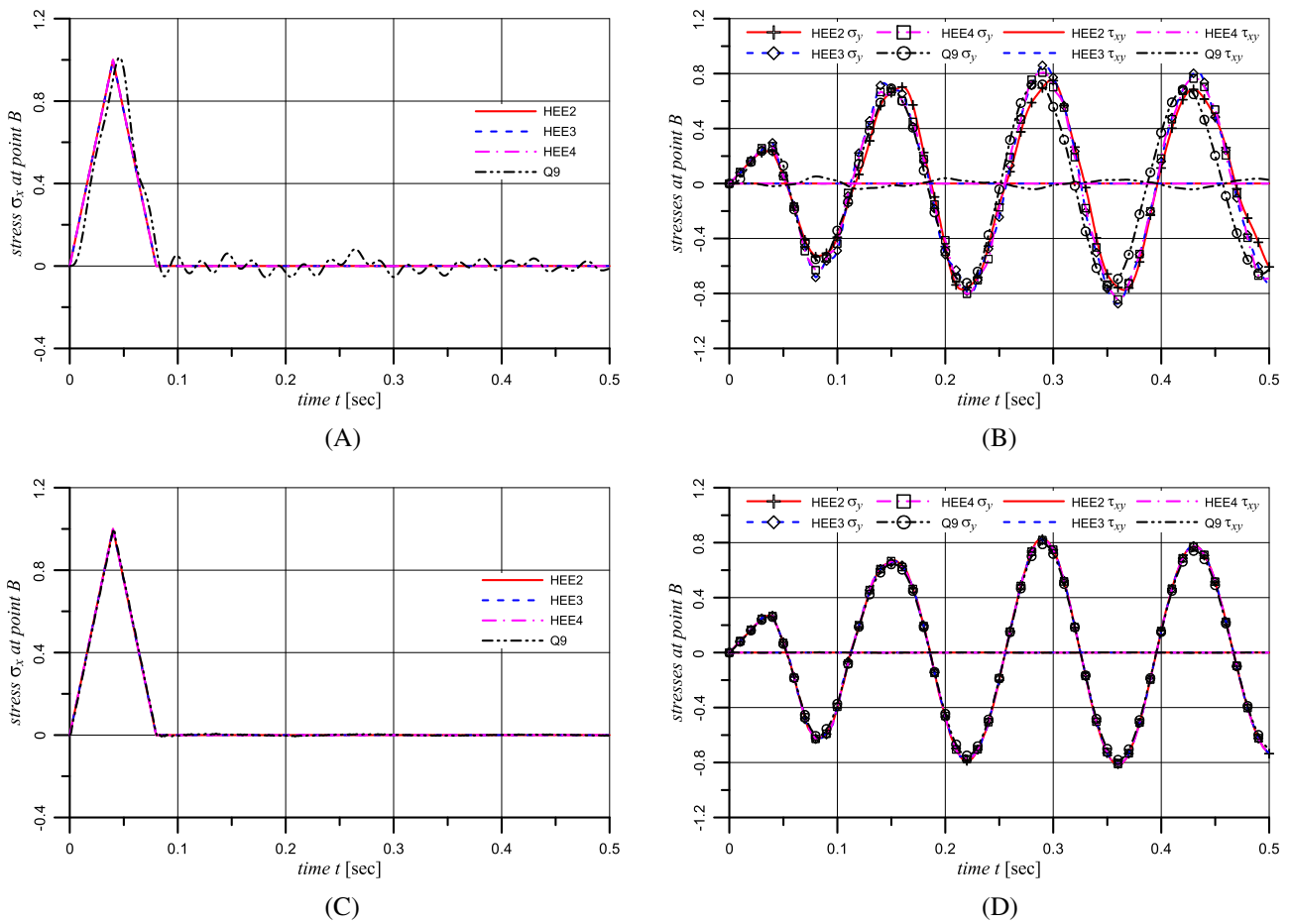
FIGURE 14   Dynamic response of a cantilever beam subjected to the fast pulse axial load $\boldsymbol{p}_n f_1(t)$ ($\Delta T = 0.08$ s), at point B in terms of (A) normal stress σ_x with coarse mesh; (B) normal stress σ_y and tangential stress τ_{xy} with coarse mesh; (C) normal stress σ_x with fine mesh; (D) normal stress σ_y and tangential stress τ_{xy} with fine mesh
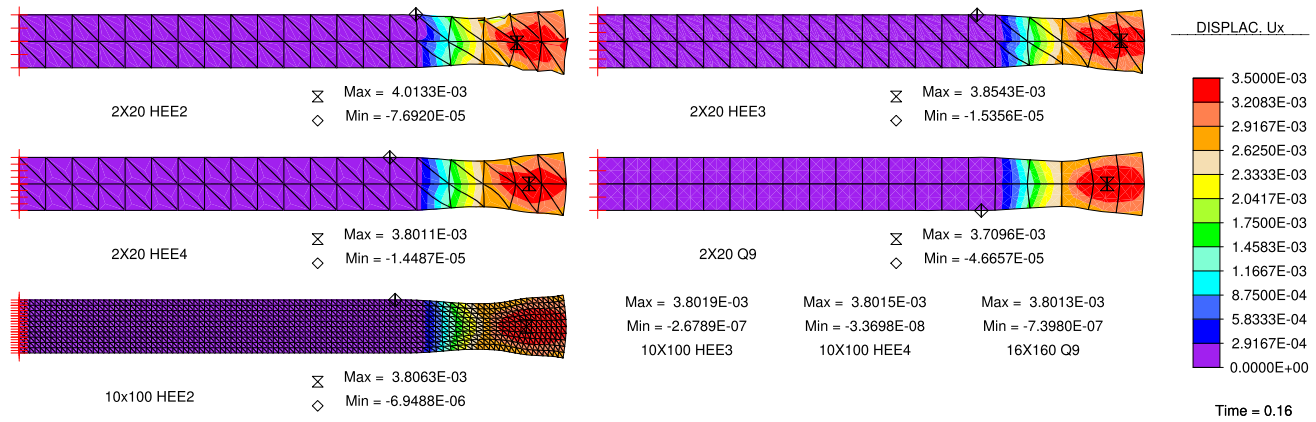
FIGURE 15 Map of horizontal displacement u_x at time $t = 0.16$ s for the cantilever beam subjected to the fast pulse axial load $\boldsymbol{p}_n f_1(t)$ ($\Delta T = 0.08$ s), computed with the quadratic, cubic, and quartic HEE and with the nine-node DB element

FIGURE 16 Map of normal stress σ_x at time $t = 0.16$ s for the cantilever beam subjected to the fast pulse axial load $\boldsymbol{p}_n f_1(t)$ ($\Delta T = 0.08$ s), computed with the quadratic, cubic, and quartic HEE and with the nine-node DB element
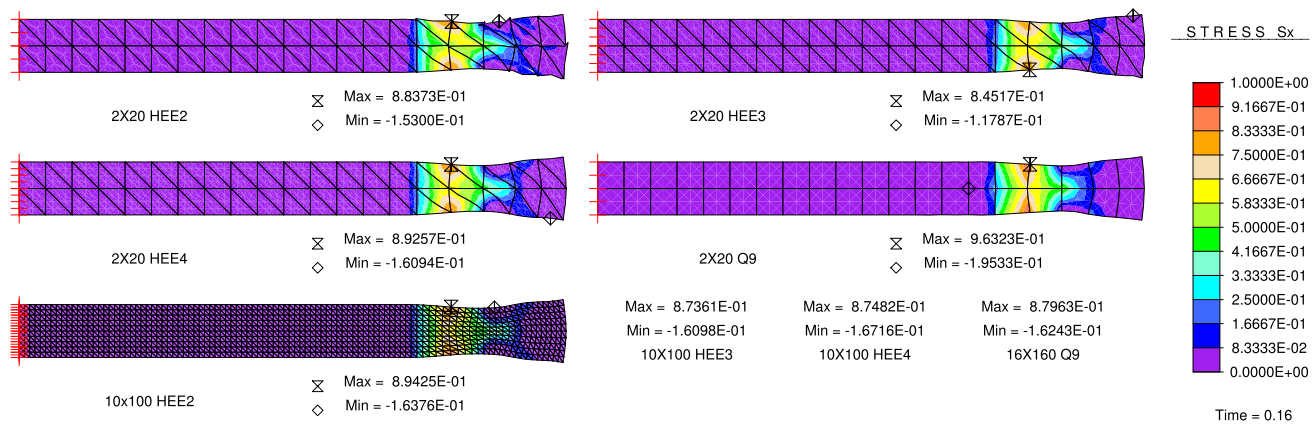
confirming the convergence of the proposed formulation and the DB approach to the exact solution. The maps of stress and displacement of the fine mesh solutions are plotted for the quadratic HEE formulation (HEE2), whereas only maximum and minimum values are reported for the other solutions, both for this numerical simulation and for the following ones.

4.2.3 | Slow tangential pulse load

Good performances of the hybrid dynamic equilibrium formulation are also found in the numerical simulation of the cantilever beam subjected to a slow and continuous pulse tangential load $\boldsymbol{p}_t f_1(t)$, with the greater value of pulse load application time: $\Delta T_1 = 8$ s, with constant time increment $\Delta t = \Delta T_1/160 = 5 \cdot 10^{-2}$ s and with $t_{max} = 50$ s. The results computed with coarse meshes are plotted in the two graphs in Figure 17 in terms of vertical displacement u_y at point A and in terms of horizontal displacement u_x at points A and B, showing negligible differences between the equilibrium-based solutions and the displacement-based one. The numerical results are also plotted in the two graphs in Figure 18 in terms of tangential stress τ_{xy} at corner A, where the exact solution is null in the whole time domain, and at point B where the quadratic tangential load imposes the stress value $\tau_{xy} = 1.5$.
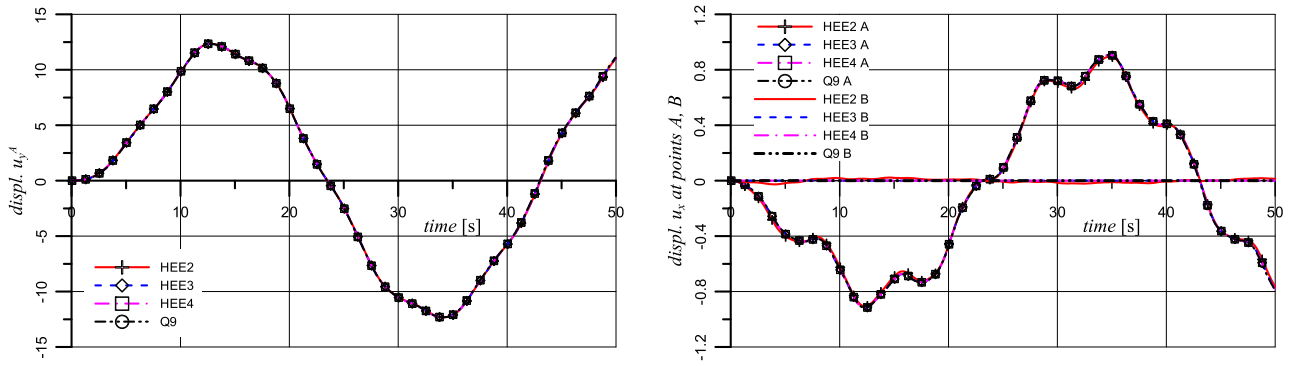
FIGURE 17 Dynamic response of a cantilever beam subjected to a slow tangential pulse load $\boldsymbol{p}_t f_1(t)$ ($\Delta T = 8$ s), in terms of vertical displacement u_y at point A, and in terms of horizontal displacement u_x at points A and B, for the quadratic, cubic, and quartic HEEs and for the nine-node DB element, with coarse 2×20 meshes
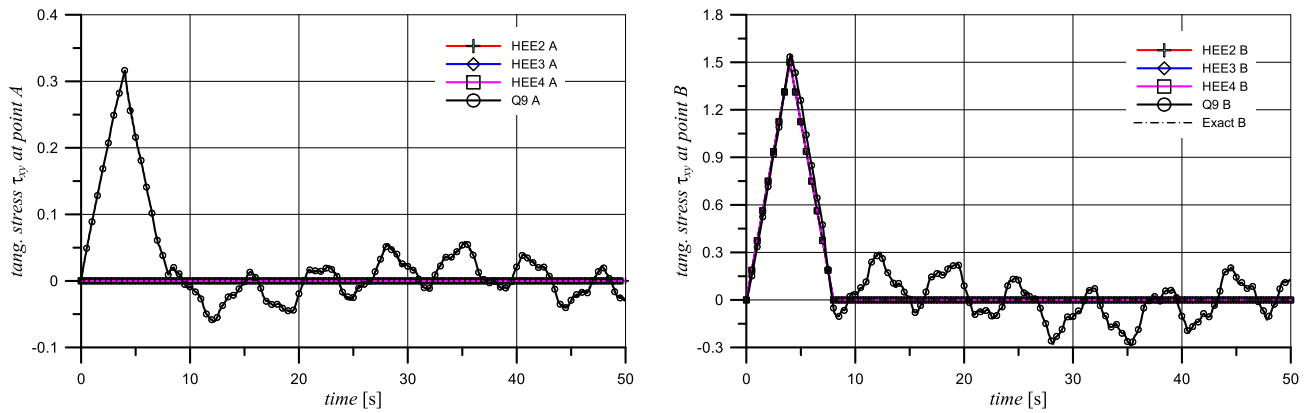

FIGURE 18 Dynamic response of a cantilever beam subjected to a slow tangential pulse load $\boldsymbol{p}_t f_1(t)$ ($\Delta T = 8$ s), in terms of tangential stress τ_{xy} at points A and B, for the quadratic, cubic, and quartic HEEs and for the nine-node DB element, with the coarse 2×10 meshes

The numerical results for a cantilever subjected to a slow pulse tangential load confirms the good results of the proposed formulation, showing some slightly incorrect values of displacement u_x at point B computed with the quadratic equilibrium formulation (HEE2). The cubic and quartic stress field equilibrium formulations produce exact values. By contrast, the equilibrium-based approach produces exact values of stresses at the free end, where tangential stress is applied as a boundary condition, and the DB solution computes incorrect values of the tangential stress for all time steps. The distribution of the three stress components at the right end at time step $t = 4$ s, computed with the coarse meshes of quadratic, cubic, and quartic equilibrium elements and with nine-node DB elements, are plotted in Figure 19. This graph clearly shows the limits of the classical DB models in stress response: linear tangential stress instead of quadratic trend; nonzero normal stress σ_x at the free end; and nonzero normal stress σ_y at the two corners. The differences between the three equilibrium formulation are due to the high order of the exact solution, which is defined by a cubic function for the normal stress component σ_y. So the quadratic formulation can reproduce only an approximate solution, whereas the cubic formulation and the quartic one can reproduce the exact solution. The numerical results are accompanied by maps of the vertical displacement and maps of the tangential stress at time step $t = 16$ s plotted respectively in Figures 20 and 21, which were computed with the four considered formulations using coarse and fine meshes.

4.2.4 | Fast tangential pulse load

Similarly to the case of axial force, the differences between the equilibrium-based and displacement-based formulations are more pronounced for the faster tangential pulse load, which is defined by the pulse tangential load $\boldsymbol{p}_t f_1(t)$, with
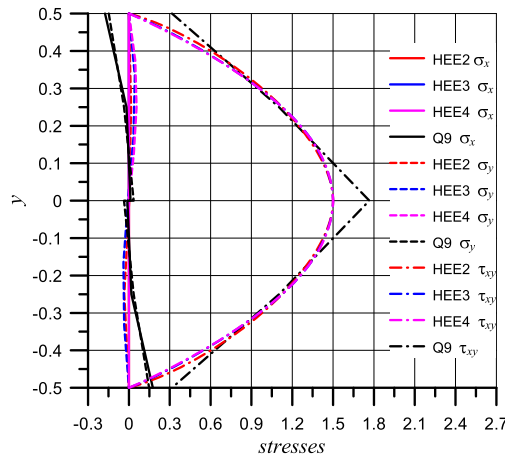
FIGURE 19 Distribution of the stress components at the right end of the cantilever beam at the step $t = 4$ s, for the quadratic, cubic, and quartic HEEs and for the nine-node DB element, with coarse 2×10 meshes
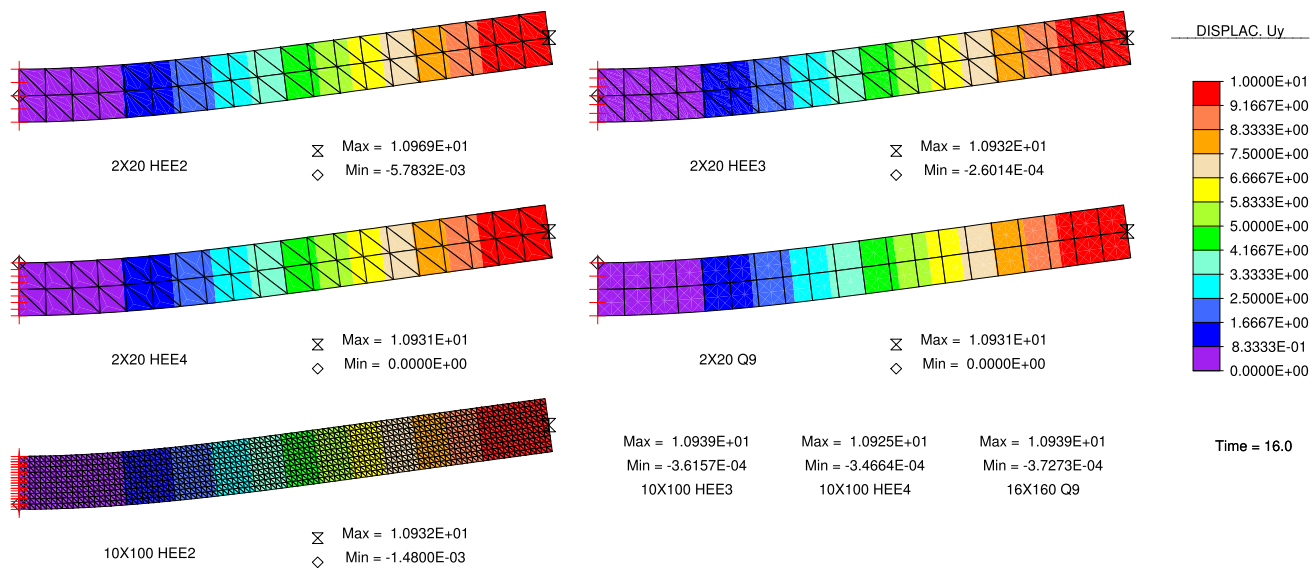
FIGURE 20 Map of vertical displacement u_y at time $t = 16$ s for a cantilever beam subjected to the slow tangential pulse load $\boldsymbol{p}_t f_1(t)$ ($\Delta T = 8$ s), computed with the quadratic, cubic, and quartic HEEs and with the nine-node DB element

the value of pulse load application time $\Delta T_2 = 0.08$ s, with constant time increment $\Delta t = \Delta T_2/160 = 5 \cdot 10^{-4}$ s and with $t_{max} = 0.5$ s. The numerical results computed with the coarse meshes are compared in the first graph in Figure 22 in terms of vertical and horizontal displacement components u_x and u_y at point A in the whole time domain, showing significant differences between the four formulations with coarse meshes, especially for the quadratic equilibrium-based one (HEE2). This differences completely disappear with fine meshes, as shown in the second graph in Figure 22, confirming the convergence of the proposed formulation to the exact solution.

The numerical results computed with coarse meshes are compared in the first graph in Figure 23 in terms of normal stress σ_x in the whole time domain at point C, where such component cannot be imposed as a boundary condition. In the same graph the stress components σ_y and τ_{xy} computed at point C with the Q9 DB approach are plotted. These stresses should be null, being components of the traction at the free boundary, whereas they are exactly computed by the equilibrium formulation. The same stress components are plotted in the second graph in Figure 23 for fine meshes, showing the convergence of the four formulations to the same solution, although some residual error can be observed in the stress components σ_y and τ_{xy} computed with the DB nine-node element.
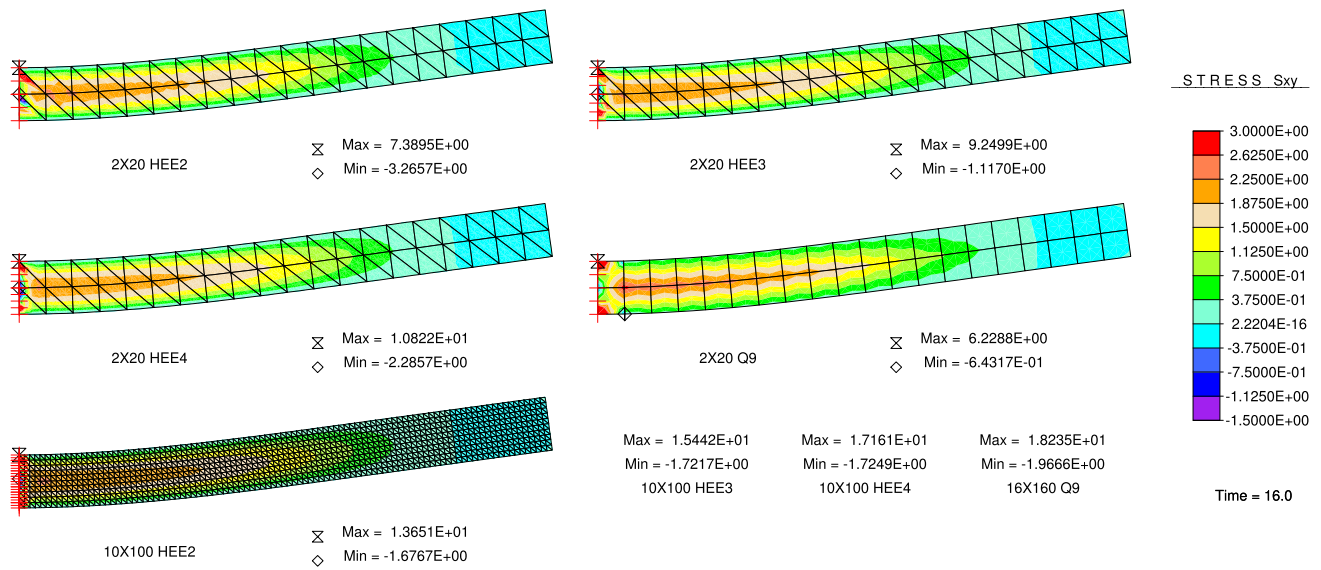
FIGURE 21 Map of tangential stress τ_{xy} at time $t = 16$ s for the cantilever beam subjected to slow tangential pulse load $\boldsymbol{p}_t f_1(t)$ ($\Delta T = 8$ s), computed with the quadratic, cubic, and quartic HEE and with the nine-node DB element
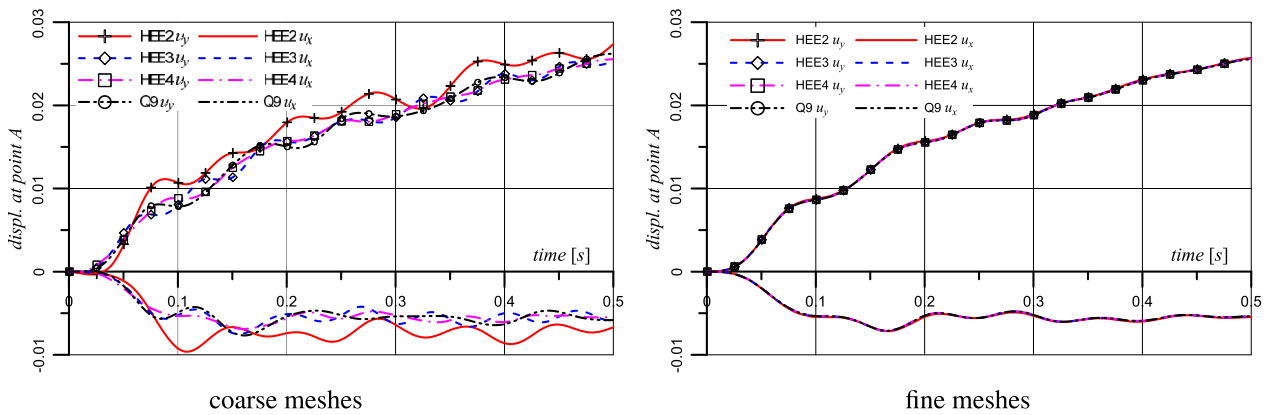

FIGURE 22 Dynamic response of a cantilever beam subjected to the fast tangential pulse load $\boldsymbol{p}_t f_1(t)$ ($\Delta T_2 = 0.08$ s) in terms of vertical and horizontal displacements u_x and u_y at point A, for the quadratic, cubic, and quartic HEEs and for the nine-node DB element
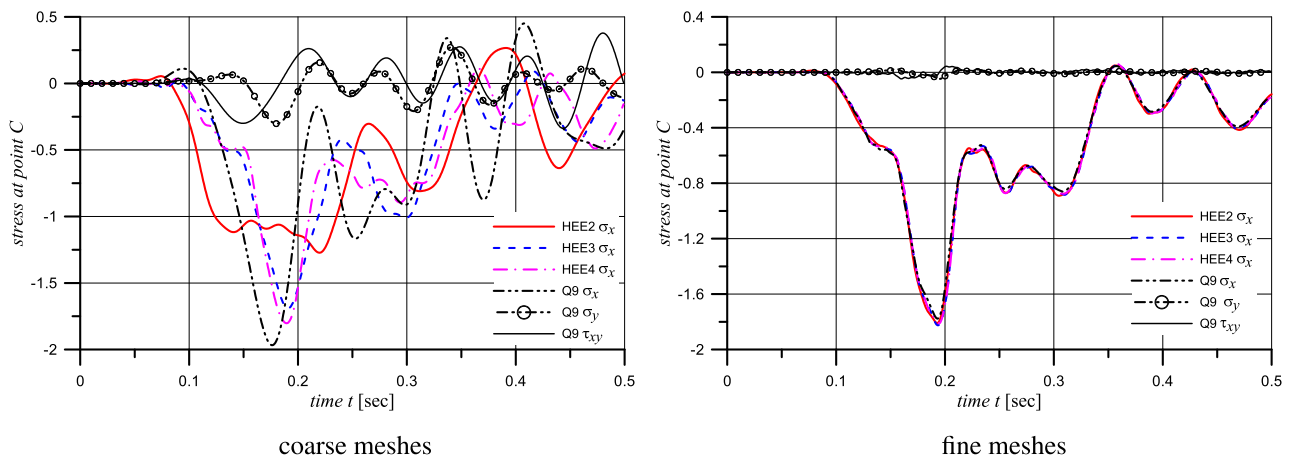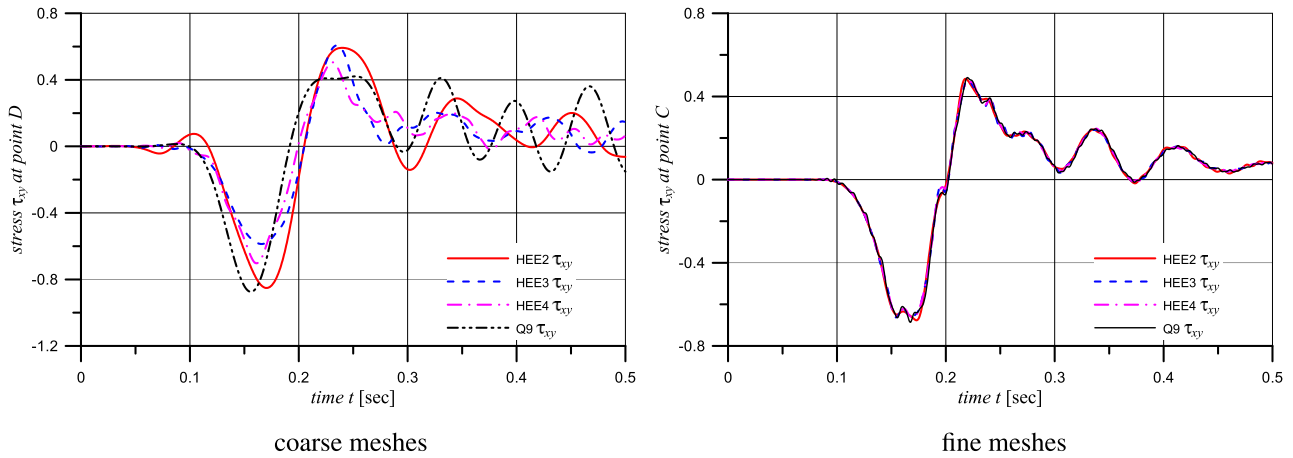

FIGURE 23 Dynamic response of a cantilever beam subjected to the fast tangential pulse load $\boldsymbol{p}_t f_1(t)$ ($\Delta T = 0.08$ s), in terms of stress components at point C for the quadratic, with the coarse and fine meshes

FIGURE 24 Dynamic response of a cantilever beam subjected to the fast tangential pulse load $p_t f_1(t)$ ($\Delta T = 0.08$ s), in terms of stress components at point D, with the coarse and fine meshes
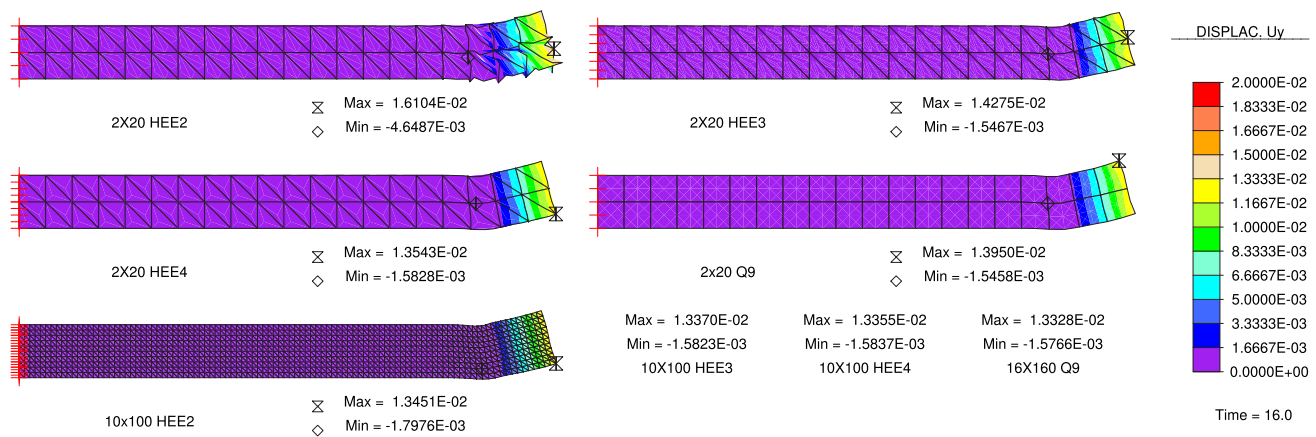
FIGURE 25 Map of vertical displacement u_y at time $t = 0.16$ s for a cantilever beam subjected to the fast tangential pulse load $p_t f_1(t)$ ($\Delta T = 0.08$ s), computed with the quadratic, cubic, and quartic HEEs and with the nine-node DB element

The trend of tangential stress τ_{xy} in the whole time domain at the internal point D, therefore not assumed as boundary condition, is plotted in the graph in Figure 24 for the coarse meshes and for the fine meshes.

The maps of vertical displacement u_y and the maps of tangential stress τ_{xy}, at time $t = 0.16$ s, computed with the HEE formulations and the DB one, with coarse and fine meshes, are plotted respectively in Figures 25 and 26. There it can be observed that some displacement discontinuity between coincident nodes is noticeable in the solution with coarse mesh and quadratic stress field (HEE2) but totally vanishes with the higher stress fields (HEE3 and HEE4) and also with fine meshes.

In order to analyze the numerical error introduced by the Newmark time integration, the numerical simulation of the cantilever beam subjected to the fast tangential pulse load is also performed with a greater time step value $dt = \Delta T_2/16 = 5 \cdot 10^{-3}$ s and with the same time domain with $t_{max} = 0.5$ s. The differences in the numerical solutions due to the greater time step are negligible with the fine meshes both for the HEE formulation and for the DB one. The greater time step does not produces any significant error neither with the coarse meshes and with comparable effects between the HEE formulation and the DB one. For the coarse meshes, the results of the numerical simulations performed with the two different values of the time step are compared in Figure 27A in terms of tangential stress at point D, and are compared in Figure 27B in terms of vertical displacement at the point A. Figure 27A,B shows that increasing the time step with the Newmark time integration method seems to produce similar effects in the HEE formulation and in the displacement based one, that is a delay in the response with an increase of the period.
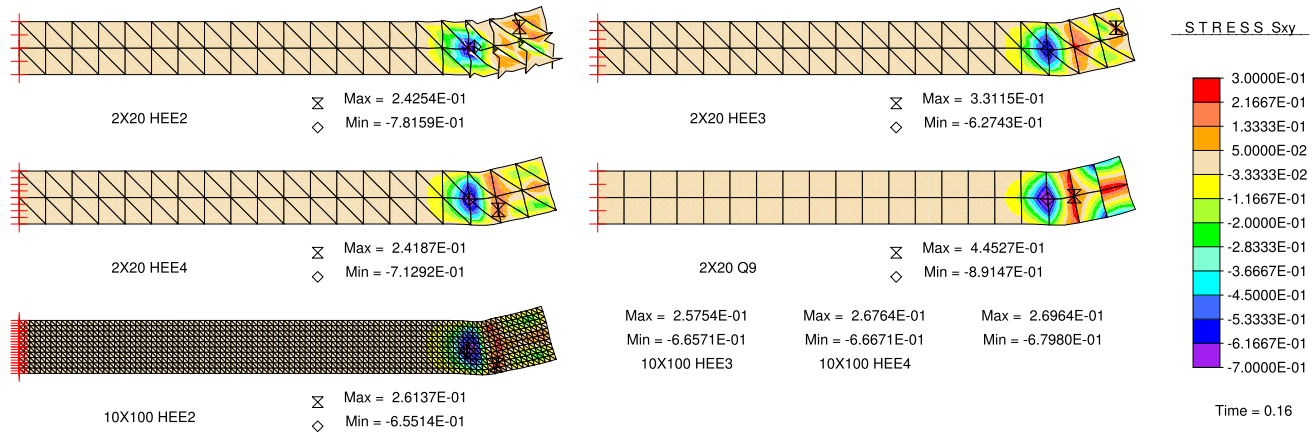
FIGURE 26 Map of tangential stress τ_{xy} at time $t = 0.16$ s for a cantilever beam subjected to the fast tangential pulse load $\boldsymbol{p}_t f_1(t)$ ($\Delta T = 0.08$ s)
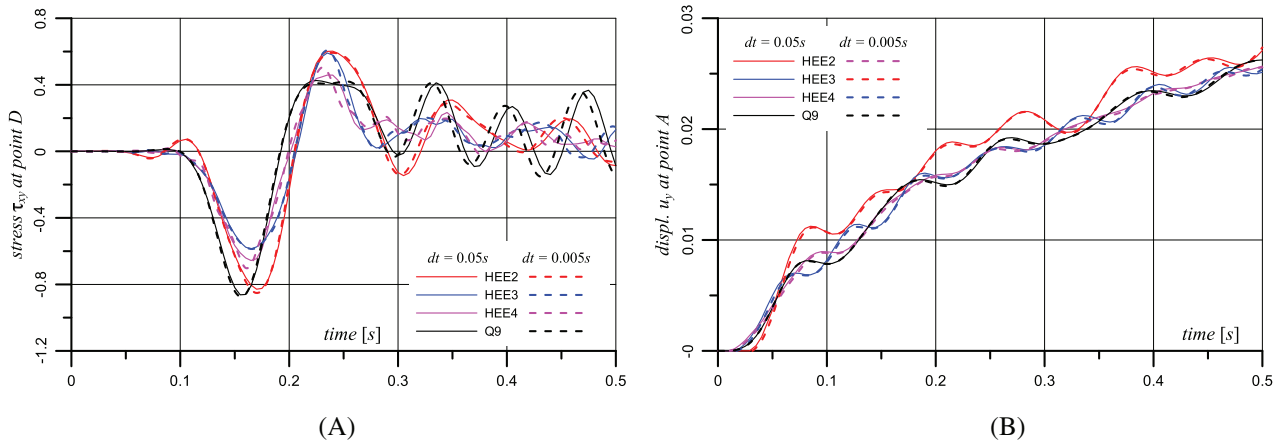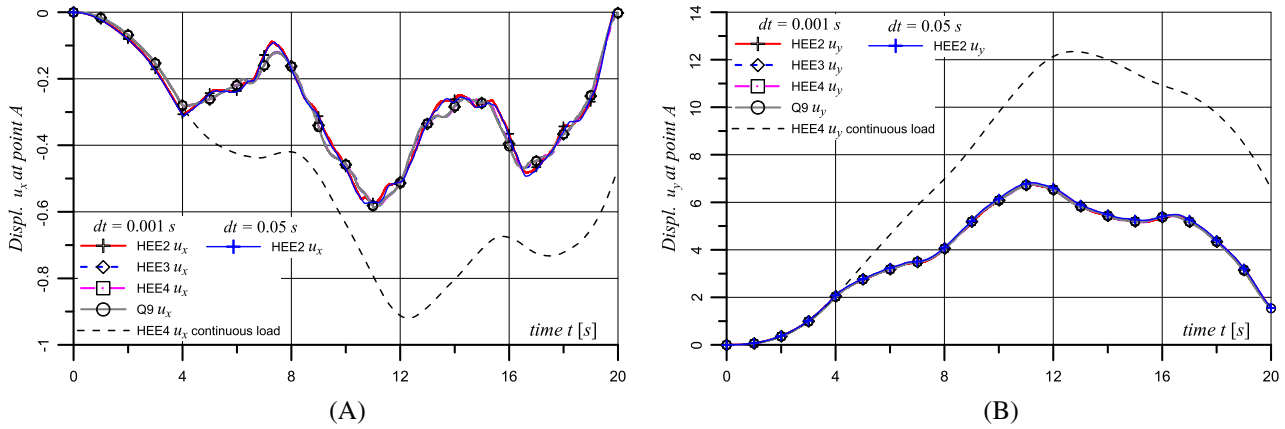

FIGURE 27 Dynamic response of a cantilever beam subjected to the fast tangential pulse load $\boldsymbol{p}_t f_1(t)$ ($\Delta T = 0.08$ s). The numerical results obtained with two different time steps ($dt = 0.05$ s and $dt = 0.005$ s) are compared in terms of (A) tangential stress τ_{xy} at point D; (B) vertical displacement at point A

4.2.5 | Slow and discontinuous tangential pulse load

The proposed hybrid equilibrium formulation and the classic DB one are also compared for the elastic-dynamic analysis of the beam cantilever subjected to the time discontinuous load, that is the tangential load $\boldsymbol{p}_t$ with the time discontinuous load function $f_2(t)$, with the value of pulse load time $\Delta T = \Delta T_1/2 = 4.0$ s and with $t_{max} = 20s$. The load discontinuity is applied in a single load step and two values of the constant time increment are considered: the standard value $dt = 0.05$ s and the very small value (compared with load application time ΔT) $dt = 0.001$ s, with a stronger discontinuity in the load time law.

The numerical results computed with the coarse meshes are plotted in the Figure 28A,B in terms of horizontal and vertical displacement u_x and u_y at point A. The results are also compared with the solution of the continuous tangential load, from which the responses diverge after the load discontinuity, and are compared with the solutions of the quadratic equilibrium formulation performed with the small time increment $dt = 0.001$ s, showing almost identical results. The numerical solutions of the discontinuous tangential load performed with the standard time increment $dt = 0.05$ s are plotted the Figure 29A in terms of tangential stress τ_{xy} at the boundary point B, showing an exact response at the load discontinuity for the HEE formulations and the approximate solution of the DB one. The tangential stress τ_{xy} at the internal

FIGURE 28 Dynamic response of a cantilever beam subjected to a discontinuous pulse tangential load $p_t f_2(t)$ ($\Delta T = 4$ s) and time increment $dt = 0.05$ s, in terms of (A) horizontal displacements u_x at point A; (B) vertical displacements u_y at point A. The results are compared with the continuous pulse load solution and to the quadratic HEE solution with the smaller time increment $dt = 0.001$ s
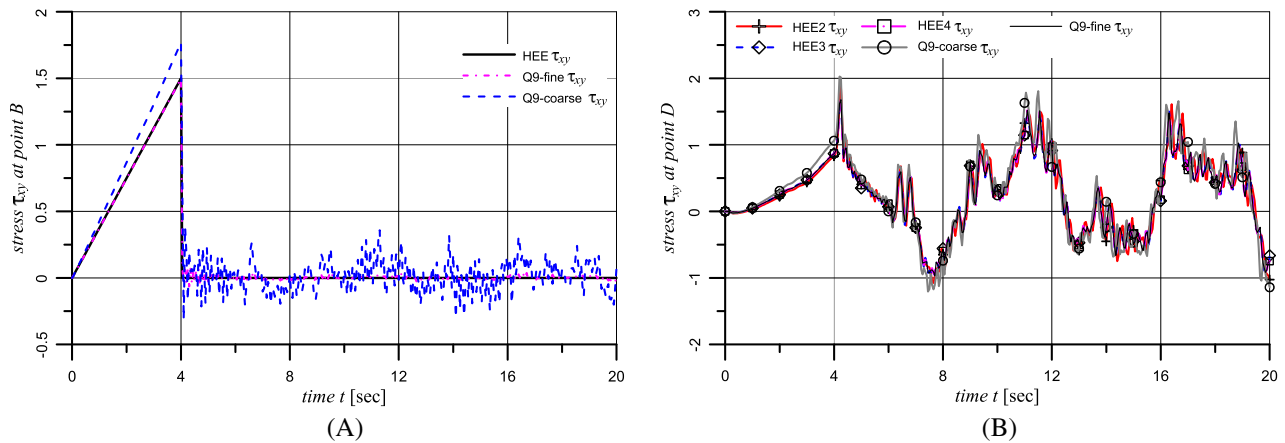
FIGURE 29 Dynamic response of a cantilever beam subjected to a discontinuous pulse tangential load $p_t f_2(t)$ ($\Delta T = 4$ s), in terms of (A) tangential stress τ_{xy} at point B; (B) tangential stress τ_{xy} at point D

point D are plotted in Figure 29B, showing very similar results, and with the equilibrium solutions almost coincident to the converged one, obtained by the DB formulation with fine mesh (Q9 element).

4.2.6 | Slow tangential pulse load for quasi-incompressible material

Finally, the last numerical simulation of a cantilever beam subjected to a dynamic pulse uniform body force $b_y = 0.1$ with a slow loading law ($\Delta T_1 = 8$ s) was performed under a plane strain quasi-incompressible condition with Poisson ratio $\nu = 0.4999$, for which the DB formulation suffers the volumetric locking numerical problem. The numerical results computed with coarse meshes are compared in the graph in Figure 30A in terms of normal stress σ_x at point C, where such component cannot be imposed as a boundary condition, and the results are compared with the converged solution obtained by the fine mesh. The numerical results are plotted in the graph in Figure 30B in terms of tangential stress τ_{xy} and normal stress σ_x at the internal point D, and the results are compared with the converged solution obtained by the fine mesh. The normal stress σ_x at point D in the exact solution is null in the whole time domain, and this result is confirmed by the HEE formulation. The two graphs also show the well-known problems of the DB formulation in evaluation of the normal stress components in quasi-incompressible elastic-dynamic problems.

The numerical results computed with coarse meshes are compared in terms of vertical displacement u_y and horizontal displacement u_x at point A in Figure 31A,B. In the same figure the results are compared with
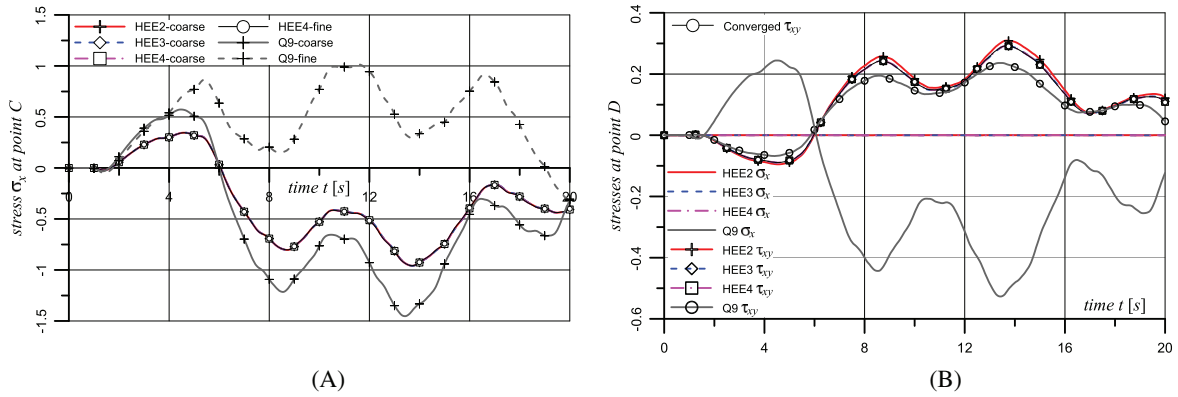
FIGURE 30 Dynamic response of a cantilever beam subjected to the pulse vertical body force load b_y with $\Delta T = 8$ s, in terms of (A) normal stress σ_x at point C; (B) normal stress σ_x and tangential stress τ_{xy} at point D

FIGURE 31 Dynamic response of a quasi-incompressible cantilever beam subjected to a uniform vertical body force load b_y with $\Delta T_1 = 8$ s in terms of (A) vertical displacement at point A; (B) horizontal displacement at point A. The results are compared with the Q9 DB numerical solution computed with the fine mesh

FIGURE 32 Map of normal stress σ_x at time $t = 16$ s for a quasi-incompressible cantilever beam subjected to a pulse vertical body force load b_y with $\Delta T_1 = 8$ s, with coarse mesh and the zoom at the constrained end with fine meshes

FIGURE 33 Map of normal stress σ_y at time $t = 16$ s for a quasi-incompressible cantilever beam subjected to a pulse vertical body force load b_y with $\Delta T_1 = 8$ s, with coarse mesh and the zoom at the constrained end with fine meshes
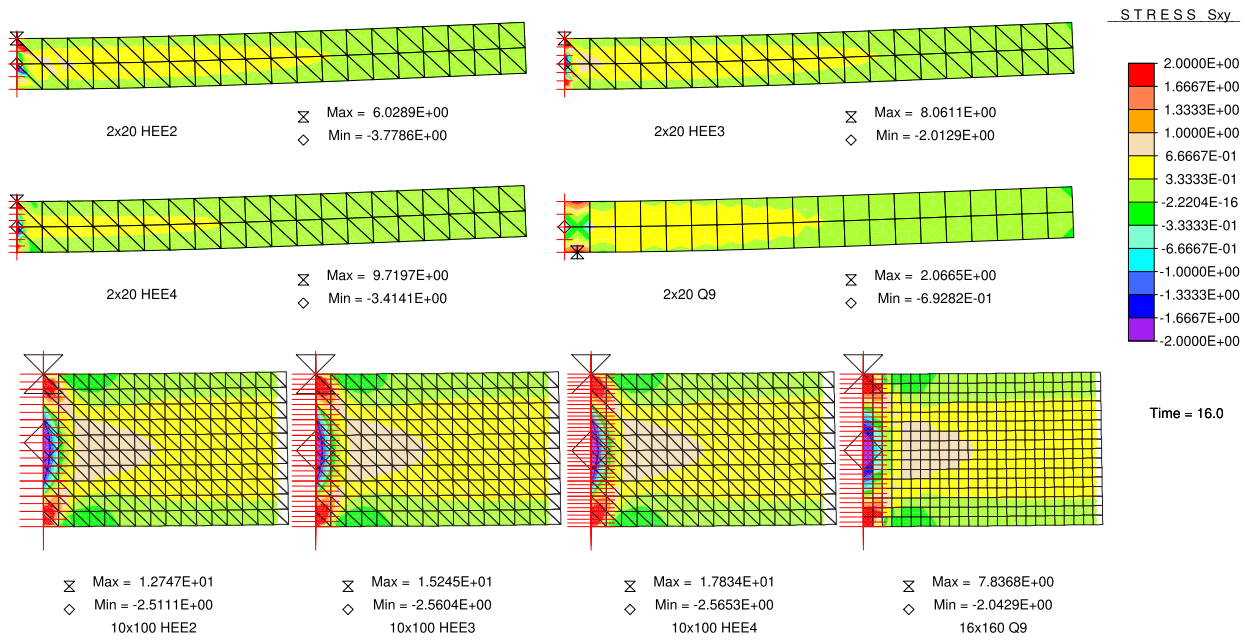
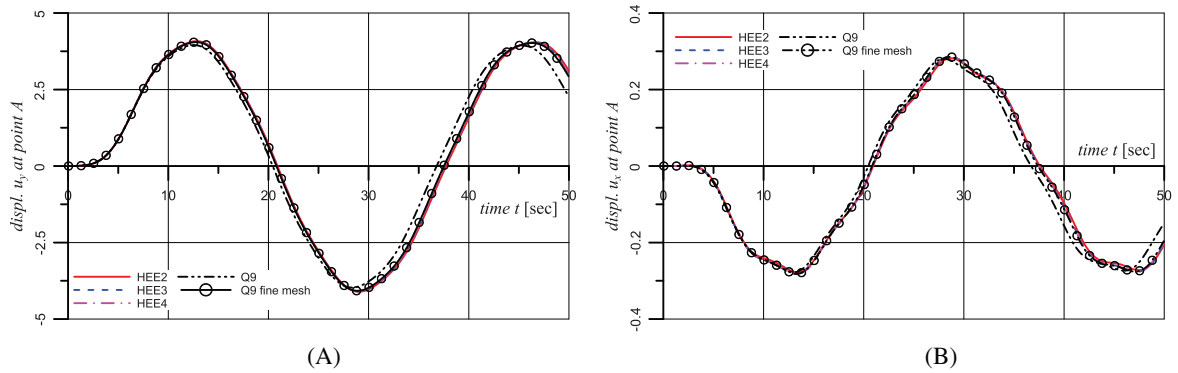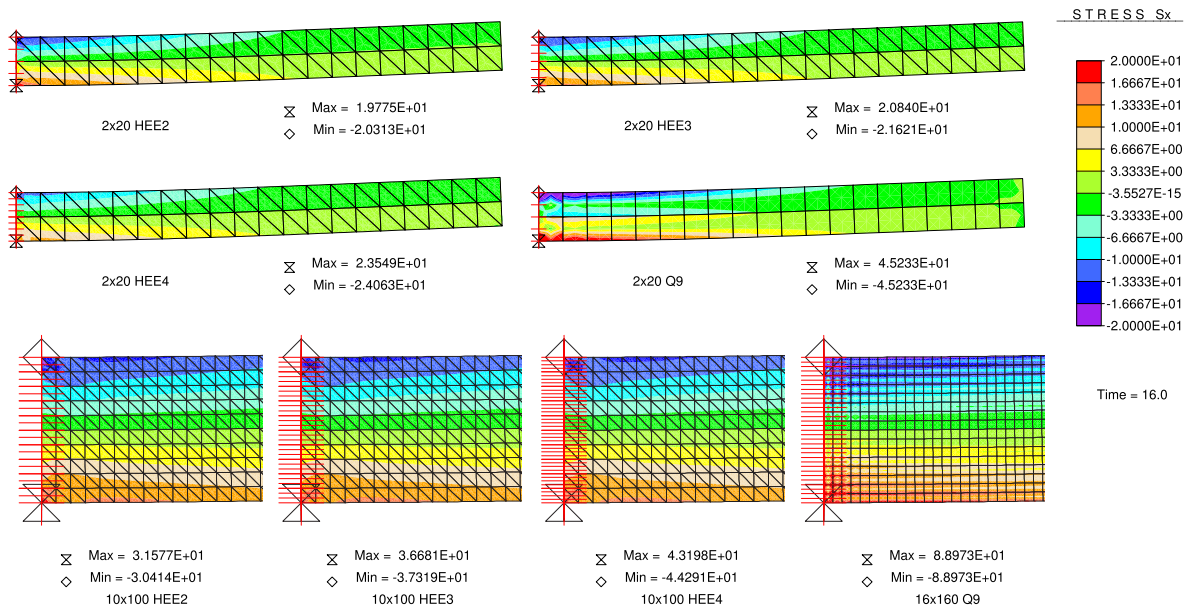**FIGURE 34** Map of tangential stress σ_{xy} at time $t = 16$ s for a quasi-incompressible cantilever beam subjected to a pulse vertical body force load b_y with $\Delta T_1 = 8$ s, with coarse mesh and the zoom at the constrained end with fine meshes
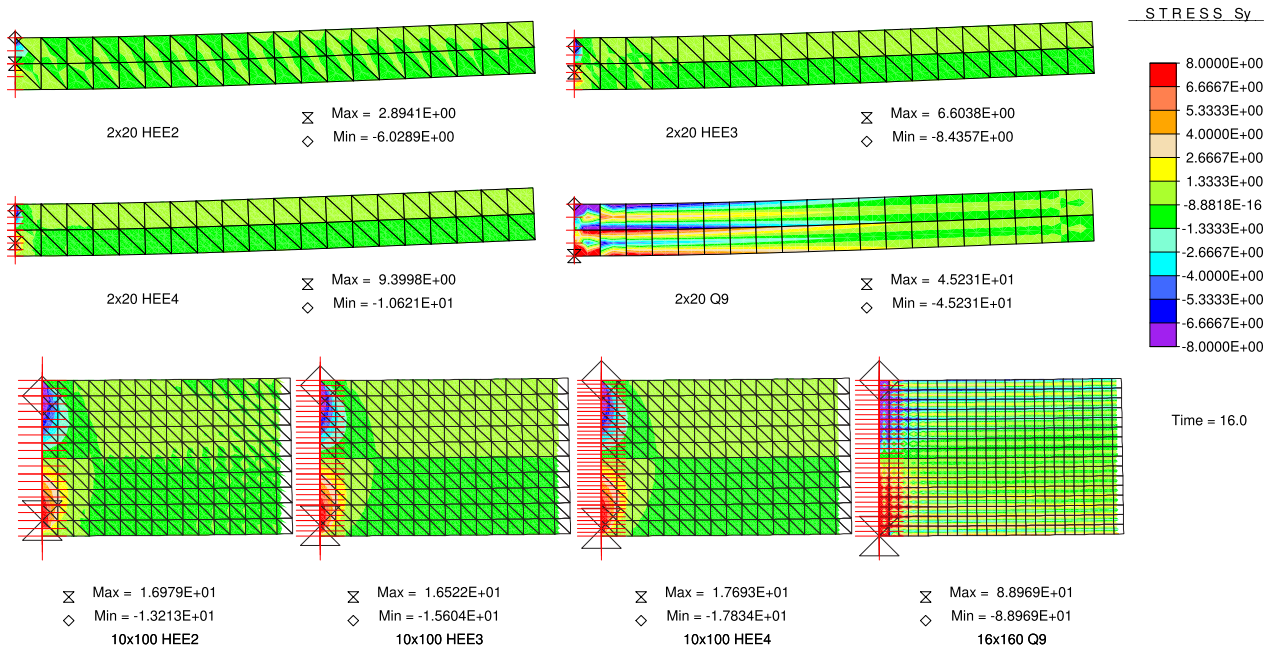
the numerical solution computed with the fine mesh of the Q9 DB formulation, and showing an excellent matching with the three solution obtained with the coarse mesh of the HEE formulation. The better performances of the proposed formulation with respect the classic DB one are clear in the maps of stresses reported in Figures 32–34, where the inconsistent stress distribution of the Q9 DB results are shown for the coarse meshes. The zoom of the constrained end of the fine-mesh solutions are plotted and clearly show the inconsistent stress gradients inside each element. Conversely, the HEE solutions are not affected by any volumetric locking.

5 | CONCLUSIONS

The present article develops the two-dimensional hybrid equilibrium element formulation, with quadratic, cubic, and quartic stress fields, for accurate static and dynamic analyses of both compressible solids and quasi-incompressible ones. The formulation is developed in the variational framework of the minimum complementary energy principle for static analysis and in the variational framework of the Toupin principle, which is the complementary form of the Hamilton principle, for dynamic analysis.

The proposed formulation is defined by independent stress fields for each finite element. The interelement and free boundary equilibrium conditions are applied using a classic hybrid formulation, and an independent displacement field is defined for each element side. The solution provides stress fields which are co-diffusive between adjacent elements and in equilibrium with traction at the free boundary sides. In the static formulation the stress fields verify the domain equilibrium equations. The dynamic formulation is developed under the hypothesis of null initial condition and is based on the impulse field (time integral of stress) and the dynamic equilibrium equation provides the pointwise velocity as the integral of the inertial term. Both the static formulation and the dynamic one are defined with high-order stress field and provide very accurate solutions in terms of stress. The analysis of a Cook membrane static problem and the analysis of a cantilever beam subjected to a pulse dynamic load were performed with several meshes for both compressible and quasi-incompressible elastic material.

The great accuracy of the stress-based proposed formulation is even more evident for static and dynamic analysis of quasi-incompressible materials, for which the classic displacement based formulation comes up against the volumetric locking. Moreover, the static and dynamic HEE formulations represent powerful numerical tools for analysis of elastic solids and also for dual analysis, as well as error estimation of the solutions performed with the classic displacement-based finite element formulations. The drawback of the proposed formulation is the possible presence of spurious kinematic modes, but they are well known and can be controlled or restrained by means of some different approaches.

The main future development of the proposed formulation could be modeling of the interelement fracture and fragmentation phenomena under dynamic load condition, through the approach proposed by the author in Reference 10, where an extrinsic (initially rigid) cohesive interface is embedded at any element side without any remeshing and without additional degrees of freedom. The extrinsic interface can activate once the stress based damaging condition is attained at the element side and the initially rigid behavior of the embedded interfaces does not affect the dynamic response of the pristine material. Conversely, the classic intrinsic interface with initial elastic behavior introduces additional compliance in the overall elastic behavior of a solid with relevant wave propagation issues.

Finally, the extension to nonzero initial conditions represents a basic requirement for analysis of a general elastic-dynamic problem and the static and dynamic analyses of pure incompressible elastic problem represent an interesting topic for further development of the HEE formulation.

CONFLICT OF INTEREST
The authors declare no potential conflict of interests.

DATA AVAILABILITY STATEMENT
The datasets generated and analyzed during the current study are available from the corresponding author on reasonable request.

ORCID
Francesco Parrinello https://orcid.org/0000-0002-9511-7177

REFERENCES
1. Fraeijs de Veubeke B. *Upper and Lower Bounds in Matrix Structural Analysis*. Vol 72. Liège, Belgium: LTAS; 1963:165-201.

2. Fraeijs de Veubeke B. Chapter 9. Displacement and equilibrium models in the finite element method. In: Zienkiewicz OC, Holister GS, eds. *Stress Analysis*. London, UK: Wiley; 1965.

3. de Almeida JPM, de Freitas JAT. An alternative approach to the formulation of hybrid equilibrium finite elements. *Comput Struct*. 1991;40:1043-1047.

4. Pereira OJBA. Hybrid equilibrium hexahedral elements and super-elements. *Commun Numer Methods Eng*. 2008;24:157-165.

5. de Almeida JPM, Pereira OJBA. A set of hybrid equilibrium finite element models for the analysis of three-dimensional solids. *Int J Numer Methods Eng*. 1996;39(16):2789-2802.

6. Kempeneers M, Debongnie JF, Beckers P. Pure equilibrium tetrahedral finite elements for global error estimation by dual analysis. *Int J Numer Methods Eng*. 2010;81:513-536.

7. Pereira OJBA, de Almeida JPM, Maunder EA. Adaptive methods for hybrid equilibrium finite element models. *Comput Methods Appl Mech Eng*. 1999;176:19-39.

8. de Almeida JPM, Reis J. An efficient methodology for stress-based finite element approximations in two-dimensional elasticity. *Int J Numer Methods Eng*. 2020;121(20):4649-4673. https://doi.org/10.1002/nme.6458

9. Zienkiewicz OC, Taylor RL, Zhu JZ. Chapter 10. Incompressible problems, mixed methods, and other procedures of solution. In: Zienkiewicz O, Taylor R, Zhu J, eds. *The Finite Element Method: Its Basis and Fundamentals*. 7th ed. Oxford, UK: Butterworth-Heinemann; 2013:315-359.

10. Parrinello F. Hybrid equilibrium element with interelement interface for the analysis of delamination and crack propagation problems. *Int J Numer Methods Eng*. 2020. https://doi.org/10.1002/nme.6531

11. Parrinello F, Failla B, Borino G. Cohesive-frictional interface constitutive model. *Int J Solids Struct*. 2009;46(13):2680-2692.

12. Parrinello F, Marannano G, Borino G. A thermodynamically consistent cohesive-frictional interface model for mixed mode delamination. *Eng Fract Mech*. 2016;153:61-79. https://doi.org/10.1016/j.engfracmech.2015.12.001

13. Parrinello F, Borino G. Non associative damage interface model for mixed mode delamination and frictional contact. *Eur J Mech A Solids*. 2019;76:108-122.

14. Noels L, Radovitzky R. An explicit discontinuous Galerkin method for non-linear solid dynamics: formulation, parallel implementation and scalability properties. *Int J Numer Methods Eng*. 2008;74(9):1393-1420. https://doi.org/10.1002/nme.2213

15. Radovitzky R, Seagraves A, Tupek M, Noels L. A scalable 3D fracture and fragmentation algorithm based on a hybrid, discontinuous Galerkin, cohesive element method. *Comput Methods Appl Mech Eng*. 2011;200(1-4):326-344. https://doi.org/10.1016/j.cma.2010.08.014

16. Olesen K, Gervang B, Reddy JN, Gerritsma M. A higher-order equilibrium finite element method. *Int J Numer Methods Eng*. 2018;114(12):1262-1290. https://doi.org/10.1002/nme.5785

17. Zhang Y, Fisser J, Gerritsma M. A hybrid mimetic spectral element method for three-dimensional linear elasticity problems. *J Comput Phys*. 2021;433:110179. https://doi.org/10.1016/j.jcp.2021.110179

18. Parrinello F. Restraining approach for the spurious kinematic modes in hybrid equilibrium element. *Comput Mech*. 2013;52(4):885-901. https://doi.org/10.1007/s00466-013-0851-x

19. Maunder EAW, de Almeida JPM, Ramsay ACA. A general formulation of equilibrium macro-elements with control of spurious kinematic modes: the exorcism of an old curse. *Int J Numer Methods Eng*. 1996;39:3175-3194.

20. Maunder EAW, de Almeida JPM. Hybrid-equilibrium elements with control of spurious kinematic modes. *Compute Assist Mech Eng Sci*. 1997;4:587-605.

21. Wang L, Zhong H. A traction-based equilibrium finite element free from spurious kinematic modes for linear elasticity problems. *Int J Numer Methods Eng*. 2014;99(10):763-788. https://doi.org/10.1002/nme.4701

22. Fraeijs de Veubeke B. *The Dual Principles of Elastodynamics: Finite Element Applications. Technical Report*. Liége, Belgium: Université de Liége; 1971.

23. Geradin M. Special applications of Hamiltons's principle to structural dynamics. In: Glowinski R, Lions JL, Laboria I, eds. *Computing Methods in Applied Sciences and Engineering, 1977*. Vol I. Berlin/Heidelberg, Germany: Springer; 1979:222-238.

24. de Freitas JAT. Formulation of elastostatic hybrid-Trefftz stress elements. *Comput Methods Appl Mech Eng*. 1998;153(1):127-151. https://doi.org/10.1016/S0045-7825(97)00042-X

25. de Freitas JAT. Hybrid finite element formulations for elastodynamic analysis in the frequency domain. *Int J Solids Struct*. 1999;36(13):1883-1923. https://doi.org/10.1016/S0020-7683(98)00064-X

26. de Freitas JAT, Wang Z. Elastodynamic analysis with hybrid stress finite elements. *Comput Struct*. 2001;79(19):1753-1767. https://doi.org/10.1016/S0045-7949(01)00106-7

27. Wang L, Lu ZR, Liu ZQ. Complementary energy principle for elastodynamics: Free of volumetric locking. *Int J Solids Struct*. 2017;120:103-114. https://doi.org/10.1016/j.ijsolstr.2017.04.032

28. Nguyen CU, Ibrahimbegovic A. Hybrid-stress triangular finite element with enhanced performance for statics and dynamics. *Comput Methods Appl Mech Eng*. 2020;372:113381. https://doi.org/10.1016/j.cma.2020.113381

29. Nguyen CU, Ibrahimbegovic A. Visco-plasticity stress-based solid dynamics formulation and time-stepping algorithms for stiff case. *Int J Solids Struct*. 2020;196-197:154-170. https://doi.org/10.1016/j.ijsolstr.2020.04.018

30. Ervin VJ. Computational bases for RTk and BDMk on triangles. *Comput Math Appl*. 2012;64(8):2765-2774. https://doi.org/10.1016/j.camwa.2012.08.011

31. de Almeida JPM, Maunder EAW. *Equilibrium Finite Element Formulations*. Hoboken, NJ: John Wiley & Sons, Ltd; 2016.

32. de Almeida JPM, Maunder EAW. Improved eigenfrequencies of mechanical systems by combining complementary models. *Int J Numer Methods Eng*. 2018;114(12):1310-1330. https://doi.org/10.1002/nme.5787

33. Toupin RA. A variational principle for the mesh-type analysis of a mechanical system. *J Appl Mech Trans ASME*. 1952;19(2):151-152.

34. Tabarrok B. Complementary variational principles in elastodynamics. *Comput Struct*. 1984;19(1):239-246 Special Memorial Issue. https://doi.org/10.1016/0045-7949(84)90223-2

35. Maunder EAW, de Almeida JPM. The stability of stars of triangular equilibrium plate elements. *Int J Numer Methods Eng*. 2009;77:922-968.

36. Harrison HR, Nettleton T. Hamilton's principle. In: Harrison H, Nettleton T, eds. *Advanced Engineering Dynamics*. Vol 3. London, UK: Butterworth-Heinemann; 1997:46-54.

37. Zienkiewicz OC, Taylor RL. *The Finite Element Method*. 5th ed. Oxford, UK: Butterworth-Heinemann Press; 2000.

38. Cook RD. Improved two-dimensional finite element. *J Struct Div*. 1974;100(ST6):1851-1863.

39. Liu GR, Nguyen-Thoi T, Lam KY. A novel alpha finite element method (αFEM) for exact solution to mechanics problems using triangular and tetrahedral elements. *Comput Methods Appl Mech Eng*. 2008;197(45):3883-3897. https://doi.org/10.1016/j.cma.2008.03.011

40. de Almeida JPM, Maunder EAW. Recovering local equilibrium from three-dimensional compatible finite element solutions. *Int J Numer Methods Eng*. 2020;121(12):2783-2805. https://doi.org/10.1002/nme.6332

41. de Almeida JPM, Pereira OJBA. Upper bounds of the error in local quantities using equilibrated and compatible finite element solutions for linear elastic problems. *Comput Methods Appl Mech Eng*. 2006;195:279-296.

42. Wang L, Zhong H. A unified approach to strict upper and lower bounds of quantities in linear elasticity based on constitutive relation error estimation. *Comput Methods Appl Mech Eng*. 2015;286:332-353. https://doi.org/10.1016/j.cma.2014.12.003

APPENDIX A. HIGH-ORDER STATIC COEFFICIENT MATRICES

The two-dimensional stress components are defined as functions of the Cartesian coordinates in Equations (2)–(4) for the quadratic formulation and are represented in Equation (5) in the Voigt notation. The coefficient matrix $\mathbf{S}_e(\mathbf{x})$ and the vector $\mathbf{a}_e$ of the generalized stress variables are defined as follows:

$$\mathbf{S}_e(\mathbf{x}) = \begin{bmatrix} 1 & y & y^2 & 0 & 0 & 0 & 0 & 0 & -x & -x^2/2 & 0 & -2xy \\ 0 & 0 & 0 & 1 & x & x^2 & 0 & -y & 0 & -y^2/2 & -2xy & 0 \\ 0 & 0 & 0 & 0 & 0 & 0 & 1 & x & y & xy & x^2 & y^2 \end{bmatrix}, \tag{A1}$$

$$\mathbf{a}_e = \begin{bmatrix} a_1 & a_2 & a_3 & a_4 & a_5 & a_6 & a_7 & a_8 & a_9 & a_{10} & a_{11} & a_{12} \end{bmatrix}^T, \tag{A2}$$

for the quadratic formulation ($n_s = 2$, $n_a = 12$),

$$\mathbf{S}_e(\mathbf{x}) = \begin{bmatrix} 1 & y & y^2 & y^3 & 0 & 0 & 0 & 0 & 0 & 0 & -x & -x^2/2 & 0 & -2xy & -x^3/3 & -x^2y & 0 & -3xy^2 \\ 0 & 0 & 0 & 0 & 1 & x & x^2 & x^3 & 0 & -y & 0 & -y^2/2 & -2xy & 0 & -xy^2 & -y^3/3 & -3x^2y & 0 \\ 0 & 0 & 0 & 0 & 0 & 0 & 0 & 0 & 1 & x & y & xy & x^2 & y^2 & x^2y & xy^2 & x^3 & y^3 \end{bmatrix}, \tag{A3}$$

$$\mathbf{a}_e = \begin{bmatrix} a_1 & a_2 & a_3 & \ldots & a_{16} & a_{17} & a_{18}, \end{bmatrix}^T \tag{A4}$$

for the cubic formulation ($n_s = 3$, $n_a = 18$), and

$$\mathbf{S}_e(\mathbf{x}) = \begin{bmatrix} 1 & y & y^2 & y^3 & y^4 & 0 & 0 & 0 & 0 & 0 & 0 & 0 & -x & -x^2/2 & 0 & -2xy & -x^3/3 \\ 0 & 0 & 0 & 0 & 0 & 1 & x & x^2 & x^3 & x^4 & 0 & -y & 0 & -y^2/2 & -2xy & 0 & -xy^2 \\ 0 & 0 & 0 & 0 & 0 & 0 & 0 & 0 & 0 & 0 & 1 & x & y & xy & x^2 & y^2 & x^2y \end{bmatrix}$$

$$\begin{matrix} -x^2y & 0 & -3xy^2 & -x^4/4 & -2/3x^3y & -3/2x^2y^2 & 0 & -4y^3x \\ -y^3/3 & -3x^2y & 0 & -3/2x^2y^2 & -2/3y^3x & -y^4/4 & -4x^3y & 0 \\ xy^2 & x^3 & y^3 & x^3y & x^2y^2 & xy^3 & x^4 & y^4 \end{matrix} \Bigg], \tag{A5}$$

$$\mathbf{a}_e = \begin{bmatrix} a_1 & a_2 & a_3 & ... & a_{23} & a_{24} & a_{25,} \end{bmatrix}^T \tag{A6}$$

for the quartic formulation ($n_s = 4$, $n_a = 25$).

APPENDIX B. HIGH-ORDER DYNAMIC COEFFICIENT MATRICES

The two-dimensional impulse components of the elastic-dynamic problem are defined as functions of the Cartesian coordinates in Equation (30) for the quadratic formulation in the Voigt notation. For the quadratic formulation ($n_s = 2$, $n_a = 18$), the coefficient matrices $\mathbf{S}_e^{(2)}(\mathbf{x})$ is defined in Equation (30), the matrix of divergence of impulse $\mathbf{T}_e^{(2)}(\mathbf{x})$ is defined in Equation (33) and the vector of generalized variable is $\mathbf{a}_e^{(2)} = [a_1 a_2 a_3 ... a_{16} a_{17} a_{18}]$. For the cubic formulation ($n_s = 3$, $n_a = 30$) the vector of generalized variable and the coefficient matrices can be written in the following compact notation: $\mathbf{a}_e^{(3)} = \begin{bmatrix} \mathbf{a}_e^{(2)} \mathbf{a}_e^{(2-3)} \end{bmatrix}$, $\mathbf{S}_e^{(3)} = \begin{bmatrix} \mathbf{S}_e^{(2)} \mathbf{S}_e^{(2-3)} \end{bmatrix}$ and $\mathbf{T}_e^{(3)} = \begin{bmatrix} \mathbf{T}_e^{(2)} \mathbf{T}_e^{(2-3)} \end{bmatrix}$ with

$$\mathbf{a}_e^{(2-3)} = \begin{bmatrix} a_{13} & ... & a_{28} & a_{29} & a_{30} \end{bmatrix}^T, \tag{B1}$$

$$\mathbf{S}_e^{(2-3)} = \begin{bmatrix} x^3 & 0 & 0 & x^2y & 0 & 0 & x.y^2 & 0 & 0 & y^3 & 0 & 0 \\ 0 & x^3 & 0 & 0 & x^2y & 0 & 0 & x.y^2 & 0 & 0 & y^3 & 0 \\ 0 & 0 & x^3 & 0 & 0 & x^2y & 0 & 0 & xy^2 & 0 & 0 & y^3 \end{bmatrix}, \tag{B2}$$

$$\mathbf{T}_e^{(2-3)} = \begin{bmatrix} 3x^2 & 0 & 0 & 2xy & 0 & x^2 & y^2 & 0 & 2xy & 0 & 0 & 3y^2 \\ 0 & 0 & 3x^2 & 0 & x^2 & 2xy & 0 & 2xy & y^2 & 0 & 3y^2 & 0 \end{bmatrix}. \tag{B3}$$

For the quartic formulation ($n_s = 4$, $n_a = 45$) the vector of generalized variable and the coefficient matrices can be written in the following compact notation: $\mathbf{a}_e^{(4)} = \begin{bmatrix} \mathbf{a}_e^{(3)} \mathbf{a}_e^{(3-4)} \end{bmatrix}$, $\mathbf{S}_e^{(4)} = \begin{bmatrix} \mathbf{S}_e^{(3)} \mathbf{S}_e^{(3-4)} \end{bmatrix}$, and $\mathbf{T}_e^{(4)} = \begin{bmatrix} \mathbf{T}_e^{(3)} \mathbf{T}_e^{(3-4)} \end{bmatrix}$ with

$$\mathbf{a}_e^{(3-4)} = \begin{bmatrix} a_{31} & ... & a_{43} & a_{44} & a_{45} \end{bmatrix}^T, \tag{B4}$$

$$\mathbf{S}_e^{(3-4)} = \begin{bmatrix} x^4 & 0 & 0 & x^3y & 0 & 0 & x^2y^2 & 0 & 0 & xy^3 & 0 & 0 & y^4 & 0 & 0 \\ 0 & x^4 & 0 & 0 & x^3y & 0 & 0 & x^2y^2 & 0 & 0 & xy^3 & 0 & 0 & y^4 & 0 \\ 0 & 0 & x^4 & 0 & 0 & x^3y & 0 & 0 & x^2y^2 & 0 & 0 & xy^3 & 0 & 0 & y^4 \end{bmatrix}, \tag{B5}$$

$$\mathbf{T}_e^{(3-4)} = \begin{bmatrix} 4x^3 & 0 & 0 & 3x^2y & 0 & x3 & 2xy^2 & 0 & 2yx^2 & y^3 & 0 & 3xy^2 & 0 & 0 & 4y^3 \\ 0 & 0 & 4x^3 & 0 & x^3 & 3x2y & 0 & 2x^2y & 2y^2x & 0 & 3y^2x & y^3 & 0 & 4y^3 & 0 \end{bmatrix}. \tag{B6}$$